ARTICLE

Harnessing energy landscape exploration to control the buckling of cylindrical shells

J.R. Panter[1], J. Chen[2], T. Zhang[2]* & H. Kusumaatmaja[1]*

Even for relatively simple thin shell morphologies, many different buckled configurations can be stable simultaneously. Which state is observed in practice is highly sensitive to both environmental perturbations and shell imperfections. The complexity and unpredictability of postbuckling responses has therefore raised great challenges to emerging technologies exploiting buckling transitions. Here we show how the buckling landscapes can be explored through a comprehensive survey of the stable states and the transition mechanisms between them, which we demonstrate for cylindrical shells. This is achieved by combining a simple and versatile triangulated lattice model with efficient high-dimensional free-energy minimisation and transition path finding algorithms. We then introduce the method of landscape biasing to show how the landscapes can be exploited to exert control over the postbuckling response, and develop structures which are resistant to lateral perturbations. These methods now offer the potential for studying complex buckling phenomena on a range of elastic shells.

[1] Department of Physics, Durham University, South Road, Durham DH1 3LE, UK. [2] Department of Mechanical and Aerospace Engineering, Syracuse University, Syracuse, NY 13244, USA. *email: tzhang48@syr.edu; halim.kusumaatmaja@durham.ac.uk

Having shed the perception of being a purely problematic phenomenon[1], postbuckling responses are rapidly being shown to enable a broad range of emerging technologies[2–5]. Such applications include soft robotics and actuation[6,7], mechanical metamaterials[8] including origami- and kirigami-inspired designs[9], morphable soft electronics[10,11], logic gates[12], energy harvesting[13], damping devices[14], information storage[15], and bioinspired design[16]. However, in general the extreme complexity of these responses[17] has largely limited studies to investigate simple structures with very few local postbuckled states[18–21]. Predicting and controlling buckling responses on more complex structures is an open and increasingly active problem in as diverse a range of applications as mechanical engineering[3] to biological morphogenesis[22].

In the problem of cylindrical shell buckling, extreme landscape complexity arises from a combination of subcriticality, multiplicity and snaking in the postbuckled states[17]. Strong subcriticality has long been recognised in cylindrical shells, in which postbuckling states coexist with the unbuckled state in a loading interval which spans between the lower buckling load[23] and critical load (see ref.[24] for a detailed review). This means that, as has been revealed historically, cylindrical shells are capable of failing at even 20% of their critical load[25]. Furthermore, the particular sensitivity to lateral loads[26], has lead to the development of empirical predictions for the practical load bearing capacity of imperfect cylinders by National Aeronautics and Space Administration (NASA)[27]. Previously, buckled states have been elucidated by solving the von Kármán–Donnell equations relating the stress to the radial displacement in an elastic cylindrical shell, but only by assuming the solutions exhibit axial periodicity (see, e.g., refs.[28,29]), reminiscent of the diamond pattern shown by Yoshimura to enable global, inextensible buckling[30]. Similarly, group theory has also enabled the study of high-symmetry solutions[31]. However, a plethora of other postbuckling solutions exist, discussed recently in the context of spatial localisation of the elastic deformation leading to snaking (pinning) in the solution space[17].

In transforming between the large number of different postbuckling states, only the first transition capable of buckling the unbuckled cylinder has been investigated previously[32,33]. This particular transition has received significant interest, as capturing the minimum-energy pathway (MEP) enables the minimum-energy barrier to be obtained, which provides an absolute lower bound to the energy required for a compressed cylinder to buckle. An explicit link has therefore been made between the ease of single dimple formation and the sensitivity of loaded cylinders to lateral loading[32]. As important for structural applications, it has been suggested that these theoretical minimum-energy barriers can be accessed experimentally via a local probing technique for cylindrical[26,34–36] and spherical shells[37,38].

Here, we demonstrate how the buckled states and buckling transitions of complex systems can be comprehensively surveyed and controlled. Our key methodological contribution is to combine a simple and versatile triangulated lattice model for modelling the shell morphologies with efficient high-dimensional free-energy minimisation and transition path finding algorithms, in order to develop a powerful computational methodology for exploring the buckling landscapes. We begin by surveying the (meta) stable states—the free-energy minima in the landscape, before surveying how the minima transform into each other by the lowest energy routes. It is through this that we are able to verify that the local probe technique indeed accesses the true lowest energy barrier to the first transition. Extending from this, we connect all postbuckling morphologies via transition pathways, and so explore the stability landscape of cylindrical buckling. We reveal a diverse variation in the landscape properties, ranging from very simple funnel-shaped landscapes at low aspect

ratios and low compression ratios, to broad and highly complex glassy landscapes at long aspect ratios. Finally, we introduce a method to begin to exert control over the buckling landscape—landscape biasing, where we are able to stabilise or destabilise targeted features in the landscape, such as transition states and minima. This is achieved by making local modifications to the elastic spring constants in the triangular lattice model to simulate thickness modifications. Thus, the knowledge of the energy landscape proves highly complementary to experimental processes aimed at exerting postbuckling control[39–41]. We demonstrate the principle of landscape biasing by first showing how biasing against the unbuckled-single dimple transition state produces a 20% increase in buckling resistance of the unbuckled cylinder for a 1% increase in mass. We then show how biasing for a multiply dimpled state simplifies the local landscape, tripling the targeted state stability at 0% mass change.

Results

Free-energy minima. The triangular lattice model, detailed in the Methods section, discretises the shell into a triangulated mesh of extensional and angular elastic springs. Respectively, these allow for the decomposition of the total free energy into a sum of stretching and bending terms. To begin with, the stretching and bending spring constants, k^{stretch} and k^{bend}, are uniform throughout the shells. Each shell is generated with a well-defined aspect ratio $A_0 = L_0/(2R_0)$, where L_0 and R_0 are the length and radius of the cylinder when all springs assume their equilibrium configurations. When axially compressed, the shortening ratio is defined as $\lambda = L/L_0$, where L is the length of the compressed cylinder. The top and bottom edges of the cylinder are simply supported: the coordinates of the mesh are fixed, but the planes attached to the ends can bend freely. We also choose k^{stretch}, k^{bend}, and R_0 to maintain a constant dimensionless elastic control ratio $k^{\text{stretch}}R_0^2/k^{\text{bend}} = 2.5 \times 10^5$, and free energies E reported throughout are nondimensionalized such that the reduced free energy is $E_r = E/k^{\text{bend}}$. The elastic control ratio is chosen to be representative of a physical system, corresponding to an aluminium drinks can. The choice of elastic control ratio and nondimensionalization are discussed further in the Methods section.

The construction of the free-energy landscape begins by surveying the free-energy minima. To access the many different buckled states for each fixed aspect ratio A_0 and shortening ratio λ, a basin hopping step is employed prior to energy minimisation[42], detailed in the Methods section. Three characteristic cylinder morphologies are observed: unbuckled, singly dimpled and multiply dimpled, visualised in 3D and as radial displacement fields d in Fig. 1a–e, respectively.

The multiply dimpled states in Fig. 1c–e form the largest set of minima, within which is contained the often-studied morphologies of high rotational symmetry—the Yoshimura-like diamond dimpling pattern, an example of which is shown in Fig. 1d[30]. However, the largest multiply dimpled subset is the irregularly dimpled morphologies, a characteristic example of which is shown in Fig. 1e. A random perturbation applied to these cylindrical shells is therefore most likely to result in an irregularly dimpled state, showing that cylindrical shell buckling responses are inherently hard to predict.

The phase diagram in Fig. 1f summarises the minimum survey. At high λ in the phase diagram, the global free-energy configuration is the unbuckled state, indicated by black circles. Upon decreasing λ the multiply dimpled states become the global minima, indicated by red squares. The solid red line indicates the point at which the buckled and multiply dimpled states are isoenergetic, at which the shortening ratio therefore produces an axial load equal to the Maxwell load (a detailed discussion
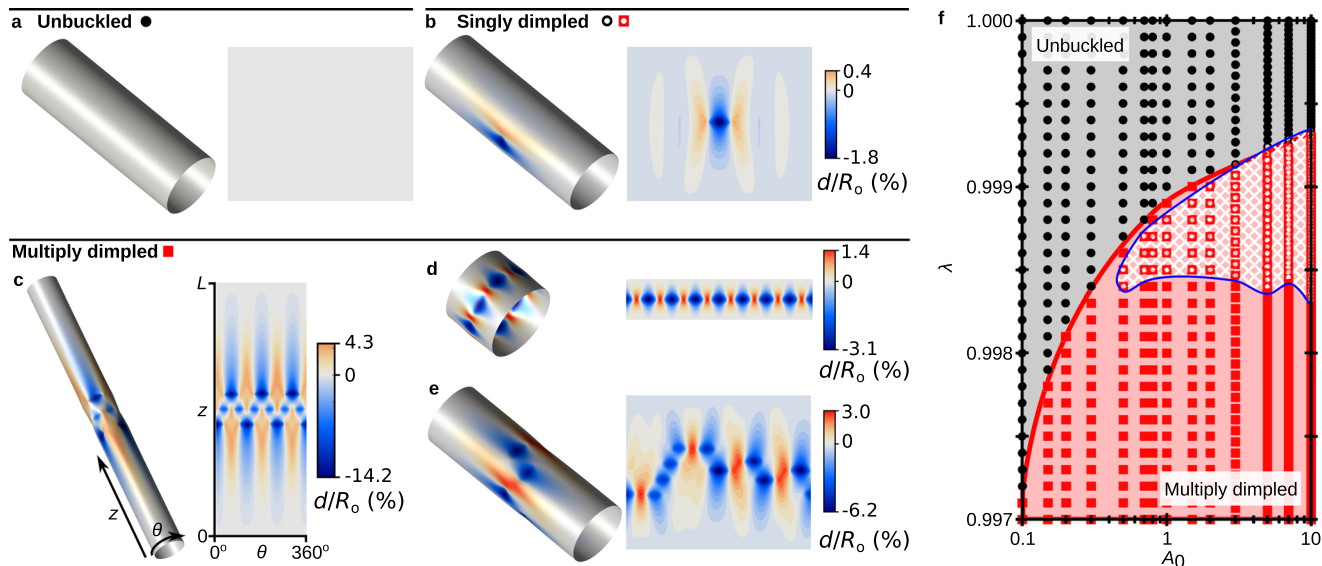
Fig. 1 Summary of the stable buckling morphology classes and the minimum-energy states. **a–e** Visualisations of representative minima, shown in 3D and as radial displacement field contour plots. The axial and angular coordinates z and θ of the contour plots are shown in (**c**), with the displacement d expressed as a fraction of R_0. **f** Phase diagram indicating the global free energy minimum across a range of aspect ratios A_0 and end shortening ratios λ. The control ratio, $k^{\text{stretch}} R_0^2 / k^{\text{bend}}$ is fixed throughout at 2.5×10^5. The global minimum is either unbuckled (grey region, simulation data shown as black circles), or multiply dimpled (pink region, simulation data shown as red squares). The singly dimpled state is never the global minimum, but the existence region is shown outlined in blue with unfilled data points.

regarding the loading limits is given in ref. [24] for example). Across all tested scenarios, the most stable multiply dimpled states are those exhibiting a high degree of rotational symmetry, most commonly those with Yoshimura-like diamond patterns. However, we also find examples where more exotic high-symmetry multiply dimpled states form the global free-energy minima, such as the example shown in Fig. 1c at $A_0 = 10$, $\lambda = 0.999$.

The singly dimpled state, shown in Fig. 1b is of significant interest due to its frequent role in the first buckling transition (which we consider further in the proceeding section), and also its characteristic role of being the unit excitation in the postbuckling landscape. However, across a broad range of aspect ratios and elastic control ratios, detailed further in Supplementary Note 1, we observed that the single dimple is never the global free-energy minimum. When it is energetically unfavourable to form a dimple, the unbuckled state is lower in energy; when it is energetically favourable to form a dimple, the energy is always lowered further by subsequent dimpling. The single dimple is therefore only metastable. This metastability region is outlined in blue in Fig. 1f. The non-monotonic form of the low-λ boundary arises from the complex deformation profile surrounding the dimple. At high aspect ratios, this profile extends around the circumference of the cylinder, such that self-interaction effects contribute to the dimple stability (detailed further in Supplementary Note 1).

Buckling transitions. In order to describe the minimum-energy mechanisms by which the cylindrical buckling morphologies interconvert, we must obtain the MEP. Between any two states in the free-energy landscape, the MEP is defined as a path in which the gradient of the free energy is parallel to the path tangent vector. The MEP will also pass through at least one saddle point in the landscape, a local energy maximum along the pathway. The buckling morphology at this point is known as the transition state. Several methods exist for finding the MEP and transition states, see for example, refs. [43–47]. The string methods we use here are detailed in the Methods section.

Computationally, the only transition which has been followed previously is the simplest unbuckled-singly dimpled pathway, where the dimple is centrally located on the cylinder[32,33]. Meanwhile, local probing of cylindrical shells has been suggested as an experimental technique which may allow the true dimpling transition state to be accessed[26,34–36]. In Fig. 2a, we compare the reduced-energy profiles $E_r(s)$ of the MEP (black series) with the pathway generated by simulating the local probe technique (blue line) for an example cylinder with $A_0 = 0.8$, $\lambda = 0.9986$. Local probe simulation methodologies are detailed in the Methods section. In order to usefully compare the paths, the path distance coordinate s is the Euclidean distance between the triangulated mesh of a point along the pathway, with that of the initial (unbuckled) state

$$s = \sum_{i=1}^{N_{\text{nodes}}} |\mathbf{a}_i - \mathbf{a}_i^o| \tag{1}$$

where $\mathbf{a}_i$ and $\mathbf{a}_i^o$ are the position vectors of node i in the buckled and unbuckled mesh, respectively.

On comparison, we observe that the local probe technique does meet the MEP at the transition state (labelled '*' and shown in Fig. 2b), but does not access the minimum-energy pathway generally. At the point of crossing the barrier, the locally-probed system snaps to a dimpled-like configuration: a small probe displacement resulting in a large change to the surrounding morphology, and a concomitant jump in E_r and s.

This comparison shows that the local probe technique is capable of measuring the minimum-energy barrier to the first dimpling transition. This is consistently shown across all the test cases summarised in Supplementary Note 2. Previous studies were unable to prove that the local probe technique could access the minimum-energy barrier, as it was assumed that the true MEP was not too curved[26]: namely the direction of motion along the transition always has a component in the direction of the applied force (i.e. the path never curves against the applied force).

However, the methodology presented here allows for the pathway between any two states to be investigated, not only
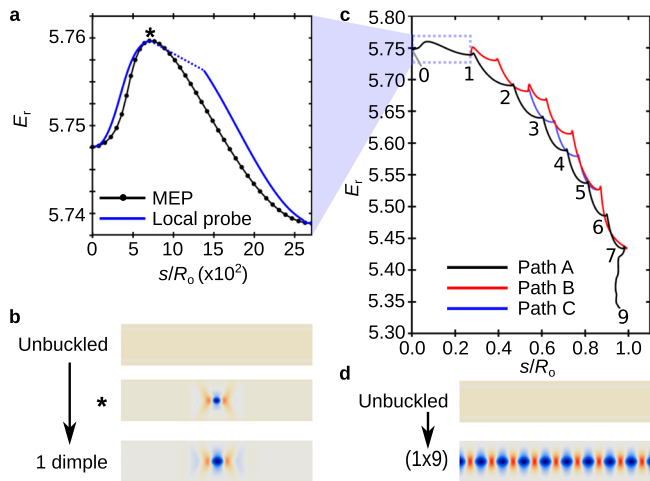
Fig. 2 Comparison of the minimum-energy pathway with the local probe technique and examples of multi-step pathways through the buckling landscape. **a** Reduced free-energy profile along the minimum-energy pathway (MEP) (black) and local probe pathway (blue) for the unbuckled-single dimple transition on a cylinder of $A_0 = 0.8$, $\lambda = 0.9986$. The end points and transition state (*) are illustrated in (**b**). The path length s describes the normalised distance of a point along the profile from the unbuckled state shown in Eq. (1). **c** Three example transition pathways connecting the unbuckled state and 1-row by 9-dimples (1×9) state illustrated in (**d**). All pathways are shown to begin with the unbuckled-single dimple transition, which is magnified in (**a**), and the number of dimples are labelled at each minimum in Path A.

the 0–1 transition. We therefore extend the first pathway found in Fig. 2a to find complete pathways from the unbuckled state to the multiply dimpled global minimum. Examples are shown in Fig. 2c, with Fig. 2d showing the pathway end points: the unbuckled state, and the (1×9) global minimum. Two key observations are made: multiple competing pathways exist between the end points and each pathway is complex, featuring many intervening minima. Out of the large number of possible pathways, three examples are highlighted in Fig. 2c, labelled A, B and C. Movies showing the conformational changes along each pathway are shown in Supplementary Movies 1, 2 and 3, respectively. Path A is distinguished from other paths: out of the set of barriers along path A, the maximum energy barrier is the smallest out of all possible pathways. In Path A, eight separate dimpling transitions occur. In the first seven, a single dimpling event occurs to build a train of dimples. The final transition sees two dimples forming simultaneously to complete the ring of nine dimples. In this final transition, the path distance decreases as all dimples become shallower on formation of the final two. However, the system is capable of undergoing dimpling transitions not linked to the growing dimple train, leading to the example alternative pathways B and C.

Energy landscapes. By connecting any pair of minima with an MEP, we may thus explore the complete energy landscape for any fixed A_0 and λ. Here we examine the extent of the landscape complexity as a function of A_0 and λ (varying the elastic constants is presented in Supplementary Note 3). As will be shown, cylindrical shells exhibit a diverse range of landscape types. We will first compare the energy landscape of a lightly compressed short cylinder where the single dimple is stable ($A_0 = 0.8$, $\lambda = 0.9986$), with a heavily compressed short cylinder where the single dimple is unstable ($A_0 = 0.8$, $\lambda = 0.9980$). We then compare the short, lightly compressed cylinder, with a long, lightly

compressed cylinder ($A_0 = 3.0$, $\lambda = 0.9990$), where the single dimple is stable in both cases.

As the network of minima connected by MEPs is in general highly complex, it is instructive to consider simplified network representations. In Fig. 3, the free-energy landscapes are visualised as disconnectivity graphs (for a comprehensive discussion of the disconnectivity graph representation of energy landscapes, we refer the reader to refs. [42,48]). In this, the network of minima and pathways is reduced to a spanning tree showing only the energy of the minima (the end points of each branch) and the lowest energy barrier connecting any two minima, read by tracing the path between two branches and finding the highest energy point. For example, in Fig. 3a, the unbuckled state and singly dimpled state are labelled '0' and '1', respectively. On tracing between the two branches, the highest energy point along the path, labelled '*' marks the largest transition state energy. In this case, this is the 0–1 transition state shown in Fig. 2b. However, as the disconnectivity graph does not show which states are directly connected, in general the highest energy point between two states is simply the largest energy encountered in the possible multi-step transition pathway.

In Fig. 3a, the disconnectivity graph is presented for $A_0 = 0.8$, $\lambda = 0.9986$, and represents the full energy landscape which was partially described in Fig. 2. Under these subcritical conditions, the unbuckled, singly dimpled, and multiply dimpled states coexist. However, the buckling landscape is remarkably simple: qualitatively, the states are (approximately) uniformly distributed across the stable energy range. To quantify this and subsequent observations, we partition the minimum-energy range into 100 bins of equal width and total the number of minima within each bin; this histogram is shown in Supplementary Note 4. We then calculate the variance in bin populations as a measure of the distribution uniformity. Here, the small variance in the bin frequency, 0.38, describes a relatively uniform distribution of minima across the energy range. The uniformity of the landscape is further reflected in the range of energy barriers—almost all have similar minimum-energy barriers of energy $\mathcal{O}(10^{-3})$. The distribution of the barriers is also shown in Supplementary Note 4.

The defective (1×8) example minimum is a characteristic state of the system, featuring clusters of dimples closely aligned around the central circumference. The (1×9) global energy minimum (highlighted in red) exists in a deep well, with the minimum-energy barrier greater than the first transition by a factor of 7. Thus, if an unbuckled state is subject to perturbations with sufficient energy to overcome the first dimpling transition, although other states may be sampled along the way, the tendency is to quickly become trapped in the global energy minimum. The notable exception to this picture, however, is that a second deep branch also exists at the base of the disconnectivity graph. This represents a competing set of deep states which are likely to split the population between the lowest minimum (1×9), and second-lowest minimum (1×8), shown in Fig. 3a.

Upon decreasing λ to 0.9980, although the system is still subcritical, the singly dimpled state loses stability. The disconnectivity graph for this landscape is shown in Fig. 3b. Here, the landscape is markedly different to the less-compressed case shown in Fig. 3a: although the number of minima is $\mathcal{O}(10)$ in both cases, at $\lambda = 0.9980$ the majority of states are concentrated at the lower stable energy range, indicated by the greater variance in bin population, 2.09, detailed further in Supplementary Note 4. In addition, the range of energy barriers is large, varying from 10^{-3} to 10^1, with many states featuring high energetic barriers. This latter point is most pronounced when considering the (2×11) multiply dimpled state, which has an energy barrier 1000× greater
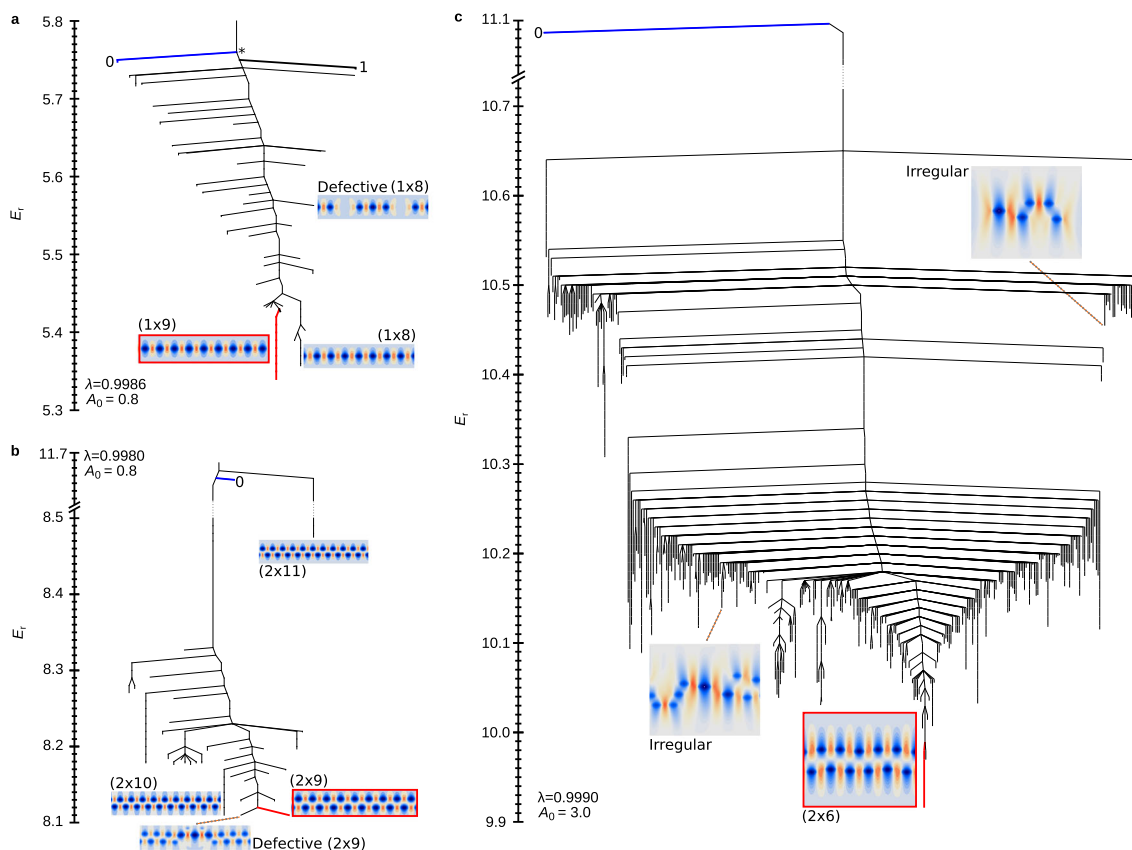
Fig. 3 Disconnectivity graphs showing the minimum energetic barrier between any pair of states. The unbuckled and global minimum branches are coloured in blue (labelled '0') and red, respectively. Representative minima radial displacement plots are also shown, with the global minimum outlined in red. **a** $A_0 = 0.8$, $\lambda = 0.9986$, the single dimple branch is labelled '1', the 0–1 transition state labelled '*'. **b** $A_0 = 0.8$, $\lambda = 0.9980$, no additional minima are present in the vertical axis break. **c** $A_0 = 3.0$, $\lambda = 0.999$, a small number of multiply dimpled states not pertinent to the discussion are present in the vertical break.

than the minimum-energy barrier from the unbuckled state. A further contrast in this disconnectivity graph is that the global minimum (2×9) does not have a large energy barrier compared to other transitions. Thus, random perturbations made to the unbuckled state may result in the system becoming trapped in several states different from the global minimum. Two highlighted examples of these which are close in energy to the global minima are the (2×10) system and a defective (2×9) system with two adjacent dimple vacancies.

Finally, we return to a subcritical shortening ratio where the unbuckled, singly dimpled, and multiply dimpled states coexist, but now extend the aspect ratio: $A_0 = 3.0$, $\lambda = 0.999$. The disconnectivity graph for this system is shown in Fig. 3c. Three prominent features of this landscape offer significant contrast to the short aspect-ratio landscapes: the number of minima has increased by a factor of 100 compared with the $A_0 = 0.8$ systems, the minimum distribution is highly non-uniform—the bin population variance is 93, and the landscape becomes rough over a range of energy scales.

Expanding on these observations, the increase in the number of minima is due to two effects. Firstly, at large aspect ratios, all minima observed are no longer characterised uniquely by a single well-defined energy and morphology, but exist as clusters in which the intra-cluster energy variability is approximately $\Delta E_r < \times 10^{-3}$. Thus, on the finest scale, the stability landscape is rough and glass-like. In the stability landscape shown in Fig. 3c, we have clustered minima which share the same number of dimples with interconversion barriers $< 10^{-3}$, reducing the

number of minima shown by a factor of 10. The second effect is due to dimple confinement introduced by the fixed ends. At $A_0 = 0.8$, the fixed ends tightly constrain the dimples to lie within either one or two rows, due to the characteristic dimple size being similar to L_0. At the longer aspect ratio of $A_0 = 3.0$, the constraining strength of the fixed ends is diminished, yielding a larger number of possibilities of dimple arrangements.

The large phase space for dimple arrangements within certain energy ranges enables numerous minima to exhibit similar energies and similar barriers. This is most pronounced in the range $10.1 < E_r < 10.3$, dominated by irregular systems with between 7 and 11 dimples. A representative irregular example is shown in Fig. 3c. In this region, the number of dimples is large enough to produce a significant number of variations in arrangement, yet not so large that packing constraints become dominant. On average, the inter-cluster energy barrier is $\mathcal{O}(10^{-2})$. A similar glassy region exists at larger energies, where irregularly dimpled systems feature between 3 and 6 dimples. A representative example is also shown here in Fig. 3c. Thus, the stability landscape becomes rough on two energy scales: (1) $\Delta E_r \approx \times 10^{-3}$ associated with intra-cluster variability, and (2) $\Delta E_r \approx \times 10^{-2}$ associated with inter-cluster variability in the absence of packing constraints (when comparing clusters of similar numbers of dimples). The distributions of energy barriers associated with this roughness are shown in the Supplementary Note 4.

For larger dimple numbers than 11, efficient packing on the cylinder is required, leading to a severe reduction in the phase

space of dimple arrangements. Thus, in the vicinity of the global minimum, the (2×6) regularly dimpled state highlighted in red, the local landscape becomes significantly less glassy. Nonetheless, the overall landscape roughness coupled with a large number of deep states means that a perturbed unbuckled cylinder may buckle to any number of states, explaining the difficulty in designing cylindrical postbuckling states.

Controlling the landscape. Despite the complexity of the buckling landscapes, we now demonstrate how to control the stability of target features, by introducing a process we term landscape biasing. This enables us to design buckling responses by locally thickening or thinning the cylinder, complementary to experimental realisation; see for example, refs. [39–41]. We demonstrate two examples of landscape biasing, by first biasing against a target transition state, and then biasing for a target minimum. The examples shown here significantly increase the stability of the target structures to lateral perturbations. These biased structures are therefore highly suited to scenarios where sudden morphological changes would be detrimental to device performance, a key example being aeronautical applications[27]. For these examples, we apply this method to $A_0 = 0.8$, $\lambda = 0.9986$ system, for which the buckling landscape is shown in Fig. 3a.

To begin with, it is observed that the minimum-energy barrier from the unbuckled state to the singly dimpled state is small compared to both the overall landscape energy range, and other deep states, generating the extreme imperfection sensitivity of cylinders to subcritical buckling transitions. The energy profile for this transition, shown originally in Fig. 2a, is re-plotted in Fig. 4a (solid black line), in which the reduced energy is referenced to the energy of the unbuckled state, E_o. We aim to increase the energy barrier of this transition, in order to make the unbuckled cylinder more robust against lateral perturbations, by biasing the landscape against the transition state.

The landscape biasing workflow is shown in Fig. 4b–d, and detailed further in Supplementary Note 5. Firstly, as shown in Fig. 4b, we obtain the radial deformation field for the unbiased transition state (as well as that of the unbuckled state). Secondly, we compute the fractional change in local elastic potential energy E_f when transforming from the unbuckled to the transition state. It is observed that the stored elastic potential energy is highly localised about the centre of the dimple deformation. We then reason that in order to increase the energy of this transition state (and hence the barrier to the transition), we must modify the cylinder to energetically penalise this localisation of the potential energy, effectively biasing the landscape against the transition state. A choice exists in how to perform this modification, but for this example we choose to simulate a local thickening of the shell by modifying k^{stretch} $(\propto t)$ and k^{bend} $(\propto t^3)$, facilitating experimental realisation. A more sophisticated yet complex treatment would alter k^{stretch} and k^{bend} independently, according to the separate local stretching and bending energies, respectively. A comparison of alternative geometric methods to modify cylindrical shell buckling are presented in ref. [39]. In the local thickening treatment, detailed in Supplementary Note 5, we weight the thickening according to the local energy change. Due to the symmetry breaking of the transition, in order to suppress dimple formation anywhere around the circumference of the cylinder, at each z we average the thickening profile over all θ. Finally, the thickening profile is rescaled in order to achieve a prescribed total mass increase, which is set as 1% for the results presented in Fig. 4. The final thickening profile is shown in Fig. 4d, which sees the a thickness increase localised around the centre of the cylinder.

On attempting to dimple this biased cylinder, the transition state is now forced off-centre, shown in Fig. 4e. The energy profile for this transition is shown as the solid red line in Fig. 4, showing that for a 1% increase in mass, a 20% increase in buckling resistance is achieved. This improvement is over twice that of a uniformly thickened cylinder, 9%, with the same mass increase, the transition profile for which is shown as the dotted black line. This landscape biasing against the transition is the antithesis to modal nudging[49], the recently formalised technique for slender structures in which minimal structural modifications are made in order to select a specific failure mode.

The second way to design the bucking landscape is to bias for a target structure. We observe the landscape shown in Fig. 3a to exhibit a deep global minimum (1×9) and the shallower (1×8) state. Here, we choose to stabilise the (1×8) state through minimum-targeted landscape biasing. It will be shown how a target minimum can be significantly stabilised, thus realising a postbuckled state which is highly resistant to lateral perturbation. Furthermore, this example will show that through biasing we can select which high-symmetry morphology forms the global minimum.

In Fig. 5a, we show the radial displacement field of the (1×8) state. As before, we evaluate the local stored elastic potential energy, then weight the local elastic constants to exact a local thickening, detailed further in Supplementary Note 5. As the (1×8) state is to be stabilised, in regions of high stored elastic energy we locally thin the structure to reduce the energetic cost of the specific buckling mode. We also weight the thickening so that there is no overall mass change, and prescribe a biasing amplitude—the maximum percentage change in thickness allowed. To obtain the local thickness change, we therefore scale the weighting field w shown in Fig. 5a by the biasing amplitude.

By systematically increasing the biasing amplitude from 0 to 20%, we observe how the buckling landscape changes at the bottom of the funnel, shown in Fig. 5b. At 0% bias, we show a magnification of the low-energy portion of the disconnectivity graph shown in Fig. 3a, featuring the two deep wells decorated with multiple stable minima. The wells corresponding to the (1×8) state and (1×9) state are shown highlighted in red and blue, respectively. In Fig. 5c, the percentage change in the (1×8) and (1×9) barriers are shown relative to their respective barriers at 0% bias.

On application of a 5% bias, the landscape changes significantly relative to the unbiased case: the landscape is simplified as the biasing destabilises many minima, the (1×9) state increases in energy, and the targeted (1×8) state decreases in energy to such an extent that it becomes the global minimum. Furthermore, the landscape simplification and (1×8) state stabilisation effects act cooperatively to increase the barrier out of the target (1×8) state by 207% relative to the unbiased (0%) landscape. At 10% bias, these effects are further magnified. At 20% bias, there is no further change in the lower landscape structure, but the stabilisation of the (1×8) state and destabilisation of the (1×9) state continues. This leads to an ultimate barrier increase of 302% for the (1×8) state, and barrier decrease of 91% for the (1×9) state.

Discussion

In this work, a triangular lattice model is used to evaluate the free energy of postbuckled states of elastic thin shells. This is implemented in efficient energy-minimisation and path finding algorithms in order to fully describe the buckling landscapes. Here, we have demonstrated this for the complex problem of buckling of fixed-end cylindrical shells, subject to axial compressive strains.
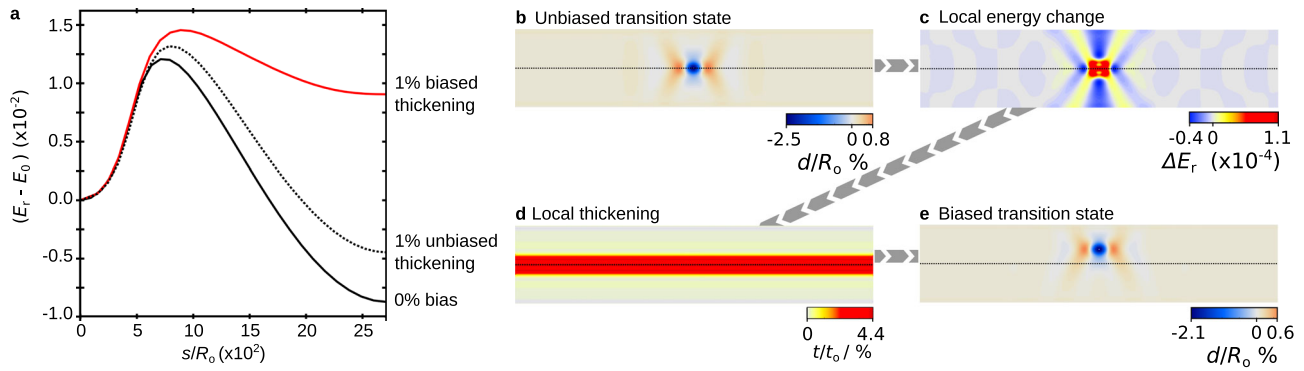
Fig. 4 The landscape biasing workflow and the effect when biasing against the unbuckled-single dimple transition state. **a** Unbuckled to single dimple transition energy profiles for three local thickening schemes: $A_0 = 0.8$, $\lambda = 0.9986$. **b**–**e** Illustrative workflow for the landscape biasing procedure, a black dotted line indicates the centre of the cylinder. **b** Radial deformation field of the unbiased transition state. **c** Local elastic potential energy change of the transition state relative to the unbuckled cylinder. **d** Local thickening profile of the 1% biased cylinder. **e** Unbuckled to single dimple transition state of the 1% biased cylinder.
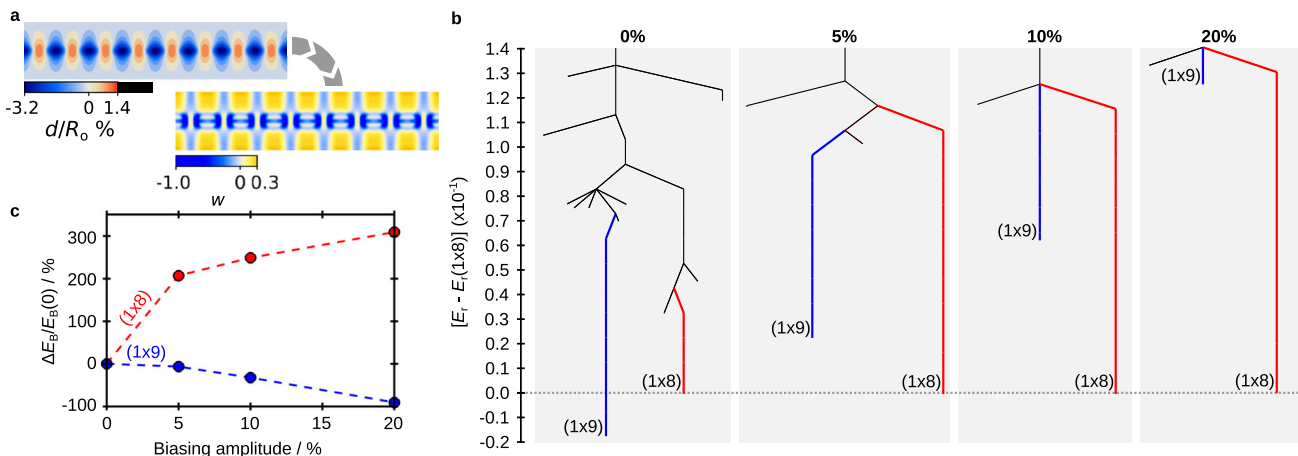
Fig. 5 Changes in the local landscape upon biasing for the (1×8) state. **a** Workflow showing how the radial deformation field of the (1×8) state at $A_0 = 0.8$, $\lambda = 0.9986$ is transformed into the thickness weighting field for landscape biasing. **b** Evolution of the bottom of the landscape as the biasing amplitude increases, all energies shown relative to the (1×8) state. The (1×8) well is highlighted in red and the (1×9) well is highlighted in blue. **c** Evolution of the change in minimum-energy barrier ΔE_B out of the (1×8) state (red), and (1×9) state (blue) upon increase in biasing amplitude. ΔE_B is shown relative to the unbiased barrier, $E_B(0)$, for the (1×8) state and (1×9) state, respectively. The dotted lines are shown as guides for the eye. Error bars associated with the convergence precision are too small to be seen, and are $<10^{-3}$%.

To begin with, we surveyed the free-energy minima, observing unbuckled, singly dimpled, and multiply dimpled states whose stabilities were evaluated for different aspect ratios and compressive strains. We then systematically used the string method to connect pairs of minima within the same cylindrical system in order to find the minimum-energy pathways and transition states between these states. This enabled a global description of the buckling landscape: in which a simple funnel-shaped landscape became complex and glassy when increasing the aspect ratio, or featured many deep states when increasing the compressive strain. We then finally introduced the landscape biasing method to control the stability of targeted features of the landscape, in order to design structures with improved resistance to lateral forces.

Overall, by being able to both survey the free-energy landscape and design specific transition modes through landscape biasing, we may now design dynamic buckling responses for diverse applications, ranging from energy harvesting devices to complex morphable materials.

One important consideration we highlight for future work is that of the role of imperfections in buckling responses, a significant concern in real-world applications. The ability to generalise our model to consider shapes other than the perfect cylinder, as well as including diverse elastic modulations and boundary conditions, lead us to emphasise the applicability of this model to studying the impact of a large range of different geometric or elastic imperfections on the buckling landscape.

Methods

Discretisation and free energy. To evaluate the free energy of an arbitrary thin shell (or composite of thin shells), we discretise the surface into a triangulated mesh of nodes, defining a set of neighbouring nodes and a set of neighbouring planes, in a manner based on ref. [50] although other similar methods have also been reported, for example, ref. [51]. The local form of this discretisation is shown in Fig. 6. In this, neighbouring nodes i and j are connected by an extensional spring of equilibrium bond length r_{ij}^0 and elastic constant k_{ij}^{stretch}. Neighbouring planes α and β are connected by an angular spring of equilibrium angle $\theta_{\alpha\beta}^0$ and elastic constant $k_{\alpha\beta}^{\text{bend}}$. In general, as in our triangulation scheme, r_{ij}^0 and $\theta_{\alpha\beta}^0$ are non-uniform across the lattice. The discretisation of the shell into a set of extensional and angular springs
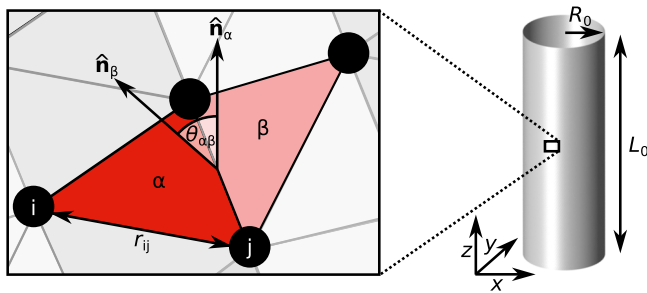
Fig. 6 The thin shell discretisation scheme. The nodes are indicated with black circles, in which nodes i and j are separated by a distance r_{ij}. The planes are indicated with coloured triangles, in which the dihedral angle between planes α and β, $\theta_{\alpha\beta}$, is shown as the angle between the respective normal vectors $\hat{\mathbf{n}}_\alpha$ and $\hat{\mathbf{n}}_\beta$.

allows the total free energy to be decomposed into a sum of stretching and bending energies such that generally,

$$E = \sum_{ij} k_{ij}^{\text{stretch}} \left(r_{ij} - r_{ij}^0 \right)^2 + \sum_{\alpha\beta} k_{\alpha\beta}^{\text{bend}} \left(1 - \cos\left(\theta_{\alpha\beta} - \theta_{\alpha\beta}^0 \right) \right), \quad (2)$$

where r_{ij} is the separation distance between nodes i and j; $\theta_{\alpha\beta}$ is the dihedral angle between planes α and β, defined as the angle between the respective normal vectors $\hat{\mathbf{n}}_\alpha$ and $\hat{\mathbf{n}}_\beta$.

Throughout this work, we report the nondimensionalised free energy $E_r = E/k_{\text{ref}}^{\text{bend}}$, where $k_{\text{ref}}^{\text{bend}}$ is a reference dihedral elastic constant. For cylinders of uniform elasticity, we define $k_{ij}^{\text{bend}} = k_{\text{ref}}^{\text{bend}}$. Furthermore, the bond lengths are nondimensionalised by expressing r_{ij} and r_{ij}^0 relative to a reference length scale R_0, which we choose to be the cylinder radius.

The single parameter defining the cylinder's elastic behaviour then becomes the control ratio $k_{\text{ref}}^{\text{stretch}} R_0^2 / k^{\text{bend}}$ which unless otherwise stated we fix at 2.5×10^5. Through comparison with continuum elastic theory[50], in terms of Young's modulus Y, plate thickness t, and Poisson ratio ν we have $k^{\text{stretch}} = \frac{\sqrt{3}}{4} Y t$ and $k^{\text{bend}} = \frac{2}{\sqrt{3}} \frac{Y t^3}{12(1-\nu^2)}$. Hence, the control ratio is given by $\frac{9(1-\nu^2)}{2} \left(\frac{R_0}{t} \right)^2$. To demonstrate the physical significance of our prescribed control ratio of 2.5×10^5, if we choose a Poisson ratio appropriate for aluminium, $\nu = 0.3$, the resulting ratio $R_0/t = 247$ is similar to that of aluminium drinks cans ($R_0/t \approx 300$).

The cylinder radius R_0 is fixed throughout, such that to change the uncompressed aspect ratio A_0, only the length L_0 is varied. In order to accurately calculate the free energy while balancing computational cost, the number of nodes must be sufficient to capture the deformation profiles of single dimples, the length scale of which depends on A_0 and the control ratio. For the cylinders studied here, $\approx 10^4$ nodes per cylinder are required (an illustrative resolution test is shown in Supplementary Note 6). Our triangulated lattice model is also validated against ABAQUS/Explicit commercial software[52], shown in Supplementary Note 7.

Minimisation and path finding. The L-BFGS algorithm[53,54] is employed to efficiently minimise the free energy with respect to the large number of degrees of freedom ($\mathcal{O}(10^4 - 10^5)$). For this, the total free energy is required as well as the derivatives of E with respect to each degree of freedom (the x, y and z coordinates of each node). By setting selected derivatives to zero prior to minimisation, we can constrain specific node positions. Here, we fix the x and y coordinates of the nodes which cap each end of the cylinder to the uncompressed configuration, forbidding deformation or relative rotation of the ends. By choosing the z coordinates at which to fix these nodes, we can achieve the desired cylinder end shortening. An example minimisation convergence plot is shown in Supplementary Note 8.

To simulate local probe experiments, in addition to fixing the end caps, we also fix the position of a single node in the centre of the cylinder (thus mimicking a point probe). This point is moved radially inwards by a small increment and the free energy is minimised. This increment-minimisation procedure is repeated until the entire pathway from the unbuckled state to a second minimum has been obtained.

In the free-energy minimum survey, we access the many different dimpled states by performing a basin hopping step prior to each minimisation[42]. To perform this step, we begin with the unbuckled cylinder, and make a random number of trial dimples to the initial node coordinates. Each trial dimple consists of a paraboloidic indentation radially into the cylinder, in which the indentation depth is allowed to vary up to $R_0/2$.

The minimum-energy pathways (MEPs) between any two minima of equal end shortening are found using the string method[55], which we augment for use with high-dimensional systems. To begin with, the end points are maximally aligned through rotation and reflection of the displacement fields. An initial string of 30

images is then formed which interpolates the coordinates of the two end points. One iteration of the algorithm consists of evolving each image in the downhill direction, then re-interpolating the images along the new string. The Euler and Runge-Kutta methods used in ref. [55] are, however, highly inefficient for the high-dimensional energy landscape considered here. Instead, we use 300 L-BFGS steps to rapidly converge the string to the MEP. A simple linear re-interpolation scheme is used, with the image density concentrated at the highest energy points along the string. This process is iterated until the E_r of the highest energy point along the string changes by $<10^{-6}$ from the previous iteration. If intermediate minima exist along the pathway, a separate string is evolved for each, such that each pathway connects two minima via a single transition state. The Euler method is employed in the final stage to fine-tune the pathway, such that convergence is achieved when the root-mean-square (RMS) distance between the strings is $<10^{-6}$. The transition state is then fine-tuned using the climbing string method with Euler steps[44], finishing once the RMS gradient is reduced below 10^{-5}. Repeating the string algorithm to connect multiple end points forms a network of connected minima.

In order to show the general validity of this model, we further apply it to analyse the energy landscapes of the buckling of spherical caps in Supplementary Note 9. Our model has similar accuracy as the finite element model implemented in ABAQUS, and successfully captures the stable axisymmetrically inverted configuration of the spherical cap[56]. The analysis is suitably rich that we reserve further discussion for another publication.

References
1. Reis, P. M., Brau, F. & Damman, P. The mechanics of slender structures. *Nat. Phys.* **14**, 1150–1151 (2018).
2. Reis, P. M. A perspective on the revival of structural (in)stability with novel opportunities for function: from buckliphobia to Buckliphilia. *J. Appl. Mech.* **82**, 111001 (2015).
3. Hu, N. & Burgueño, R. Buckling-induced smart applications: recent advances and trends. *Smart Mater. Struct.* **24**, 063001 (2015).
4. Zhang, Y. et al. Printing, folding and assembly methods for forming 3D mesostructures in advanced materials. *Nat. Rev. Mater.* **2**, 17019 (2017).
5. Bertoldi, K., Vitelli, V., Christensen, J. & van Hecke, M. Flexible mechanical metamaterials. *Nat. Rev. Mater.* **2**, 17066 (2017).
6. Rus, D. & Tolley, M. T. Design, fabrication and control of soft robots. *Nature* **521**, 467–475 (2015).
7. Hines, L., Petersen, K., Lum, G. Z. & Sitti, M. Soft actuators for small-scale robotics. *Adv. Mater.* **29**, 1603483 (2017).
8. Yang, H. & Ma, L. Multi-stable mechanical metamaterials by elastic buckling instability. *J. Mater. Sci.* **54**, 3509–3526 (2019).
9. Zhai, Z., Wang, Y. & Jiang, H. Origami-inspired, on-demand deployable and collapsible mechanical metamaterials with tunable stiffness. *Proc. Natl Acad. Sci. USA* **115**, 2032–2037 (2018).
10. Fu, H. et al. Morphable 3D mesostructures and microelectronic devices by multistable buckling mechanics. *Nat. Mater.* **17**, 268–276 (2018).
11. Ning, X. et al. Mechanically active materials in three-dimensional mesostructures. *Sci. Adv.* **4**, eaat8313 (2018).
12. Song, Y. et al. Additively manufacturable micro-mechanical logic gates. *Nat. Commun.* **10**, 882 (2019).
13. Dagdeviren, C. et al. Recent progress in flexible and stretchable piezoelectric devices for mechanical energy harvesting, sensing and actuation. *Extrem. Mech. Lett.* **9**, 269–281 (2016).
14. Haghpanah, B., Shirazi, A., Salari-Sharif, L., GuellIzard, A. & Valdevit, L. Elastic architected materials with extreme damping capacity. *Extrem. Mech. Lett.* **17**, 56–61 (2017).
15. Chung, J. Y., Vaziri, A. & Mahadevan, L. Reprogrammable Braille on an elastic shell. *Proc. Natl Acad. Sci. USA* **115**, 201722342 (2018).
16. Meyers, M. A., McKittrick, J. & Chen, P.-Y. Structural biological materials: critical mechanics-materials connections. *Science* **339**, 773–779 (2013).
17. Knobloch, E. Spatial localization in dissipative systems. *Annu. Rev. Condens. Matter Phys.* **6**, 325–359 (2015).

18. Plaut, R. H. Snap-through of arches and buckled beams under unilateral displacement control. *Int. J. Solids Struct.* **63**, 109–113 (2015).
19. Napoli, G. & Turzi, S. Snap buckling of a confined thin elastic sheet. *Proc. R. Soc. A Math. Phys. Eng. Sci.* **471**, 20150444 (2015).
20. Pandey, A., Moulton, D. E., Vella, D. & Holmes, D. P. Dynamics of snapping beams and jumping poppers. *Europhysics Lett.* **105**, 24001 (2014).
21. Forterre, Y., Skotheim, J. M., Dumais, J. & Mahadevan, L. How the Venus flytrap snaps. *Nature* **433**, 421–425 (2005).
22. Nelson, C. M. On buckling morphogenesis. *J. Biomech. Eng.* **138**, 021005 (2016).
23. vonKarman, T. & Tsien, H.-S. The buckling of thin cylindrical shells under axial compression. *J. Aeronaut. Sci.* **8**, 303–312 (1941).
24. Thompson, J. M. T. Advances in shell buckling: theory and experiments. *Int. J. Bifurc. Chaos* **25**, 1530001 (2015).
25. Seide, P., Weingarten, V. I. & Morgan, E. J. *The Development of Design Criteria for Elastic Stability of Thin Shell Structures* (Space Technology Laboratories, Inc., Los Angeles, CA, 1960).
26. Thompson, J. M. T. & Sieber, J. Shock-sensitivity in shell-like structures: with simulations of spherical shell Buckling. *Int. J. Bifurc. Chaos* **26**, 1630003 (2016).
27. NASA. *Buckling of Thin-walled Circular Cylinders*. NASA Space Vehicle Design Criteria, Technical Report No. NASA SP-8007 (National Aeronautics and Space Administration, Washington, DC, 1965).
28. Lord, G. J., Champneys, A. R. & Hunt, G. W. Computation of localized post buckling in long axially compressed cylindrical shells. *Philos. Trans. R. Soc. A Math. Phys. Eng. Sci.* **355**, 2137–2150 (1997).
29. Hunt, G. W. et al. Cellular buckling in long structures. *Nonlinear Dyn.* **21**, 3–29 (2000).
30. Yoshimura, Y. *On the Mechanism of Buckling of a Circular Cylindrical Shell Under Axial Compression* (National Advisory Committee for Aeronautics, Washington, DC, 1955).
31. Wohlever, J. & Healey, T. A group theoretic approach to the global bifurcation analysis of an axially compressed cylindrical shell. *Comput. Methods Appl. Mech. Eng.* **122**, 315–349 (1995).
32. Horák, J., Lord, G. J. & Peletier, M. A. Cylinder buckling: the mountain pass as an organizing center. *SIAM J. Appl. Math.* **66**, 1793–1824 (2006).
33. Kreilos, T. & Schneider, T. M. Fully localized post-buckling states of cylindrical shells under axial compression. *Proc. R. Soc. A Math. Phys. Eng. Sci.* **473**, 20170177 (2017).
34. Virot, E., Kreilos, T., Schneider, T. M. & Rubinstein, S. M. Stability landscape of shell buckling. *Phys. Rev. Lett.* **119**, 224101 (2017).
35. Gerasimidis, S., Virot, E., Hutchinson, J. W. & Rubinstein, S. M. On establishing buckling knockdowns for imperfection-sensitive shell structures. *J. Appl. Mech.* **85**, 091010 (2018).
36. Thompson, J. M. T., Hutchinson, J. W. & Sieber, J. Probing shells against buckling: a nondestructive technique for laboratory testing. *Int. J. Bifurc. Chaos* **27**, 1730048 (2017).
37. Hutchinson, J. W. & Thompson, J. M. T. Nonlinear buckling interaction for spherical shells subject to pressure and probing forces. *J. Appl. Mech.* **84**, 061001 (2017).
38. Hutchinson, J. W. & Thompson, J. M. T. Nonlinear buckling interaction for spherical shells subject to pressure and probing forces. *J. Appl. Mech.* **84**, 061001 (2017).
39. Hu, N. & Burgueño, R. Tailoring the elastic postbuckling response of cylindrical shells: a route for exploiting instabilities in materials and mechanical systems. *Extrem. Mech. Lett.* **4**, 103–110 (2015).
40. Hu, N. & Burgueño, R. Harnessing seeded geometric imperfection to design cylindrical shells with tunable elastic postbuckling behavior. *J. Appl. Mech.* **84**, 011003 (2016).
41. Kuang, X. et al. Grayscale digital light processing 3D printing for highly functionally graded materials. *Sci. Adv.* **5**, eaav5790 (2019).
42. Wales, D. J. *Energy Landscapes*. (Cambridge University Press, Cambridge, 2003).
43. Sheppard, D., Terrell, R. & Henkelman, G. Optimization methods for finding minimum energy paths. *J. Chem. Phys.* **128**, 134106 (2008).
44. Ren, W. & Vanden-Eijnden, E. A climbing string method for saddle point search. *J. Chem. Phys.* **138**, 134105 (2013).
45. Trygubenko, Sa & Wales, D. J. A doubly nudged elastic band method for finding transition states. *J. Chem. Phys.* **120**, 2082–2094 (2004).
46. Henkelman, G. & Jónsson, H. Improved tangent estimate in the nudged elastic band method for finding minimum energy paths and saddle points. *J. Chem. Phys.* **113**, 9978–9985 (2000).
47. Kusumaatmaja, H. Surveying the free energy landscapes of continuum models: application to soft matter systems. *J. Chem. Phys.* **142**, 124112 (2015).
48. Wales, D. J., Miller, M. A. & Walsh, T. R. Archetypal energy landscapes. *Nature* **394**, 758–760 (1998).
49. Cox, B., Groh, R., Avitabile, D. & Pirrera, A. Modal nudging in nonlinear elasticity: tailoring the elastic post-buckling behaviour of engineering structures. *J. Mech. Phys. Solids* **116**, 135–149 (2018).
50. Seung, H. S. & Nelson, D. R. Defects in flexible membranes with crystalline order. *Phys. Rev. A* **38**, 1005–1018 (1988).
51. Liu, K. & Paulino, G. H. Nonlinear mechanics of non-rigid origami: an efficient computational approach. *Proc. R. Soc. A Math. Phys. Eng. Sci.* **473**, 20170348 (2017).
52. Hibbitt, K. *ABAQUS/Explicit: User's Manual*, Vol. 1 (Sorenson Incorporated, 2001).
53. Nocedal, J. Updating quasi-Newton matrices with limited storage. *Math. Comp.* **35**, 773–782 (1980).
54. Liu, D. & Nocedal, J. On the limited memory BFGS method for large scale optimization. *Math. Program.* **45**, 503–528 (1989).
55. Weinan, E., Ren, W. & Vanden-Eijnden, E. Simplified and improved string method for computing the minimum energy paths in barrier-crossing events. *J. Chem. Phys.* **126**, 164103 (2007).
56. Taffetani, M., Jiang, X., Holmes, D. P. & Vella, D. Static bistability of spherical caps. *Proc. R. Soc. A Math. Phys. Eng. Sci.* **474**, 20170910 (2018).

Acknowledgements

Author contributions

H.K. and T.Z. conceived the idea, designed the research and supervised the project. J.R.P. developed the energy landscape code, and performed simulations for exploring and controlling the buckling landscapes of thin shells. J.C. developed the triangulated lattice model, benchmarked it against ABAQUS, and performed simulations for local probe tests of shells. H.K. and J.R.P. drafted the manuscript and all authors contributed to the writing of the paper.

Competing interests

The authors declare no competing interests.

Additional information

Supplementary information is available for this paper at https://doi.org/10.1038/s42005-019-0251-4.

Correspondence and requests for materials should be addressed to T.Z. or H.K.

Reprints and permission information is available at http://www.nature.com/reprints

Publisher's note Springer Nature remains neutral with regard to jurisdictional claims in published maps and institutional affiliations.